





RESEARCH ARTICLE | APRIL 21 2025

Quantitative phase imaging with a multimode fiber

Aleksandra Ivanina; Maxim Marshall ; Ksenia Abrashitova; Tristan van Leeuwen ;
Lyubov V. Amitonova  



APL Photonics 10, 046116 (2025)

<https://doi.org/10.1063/5.0253648>



Articles You May Be Interested In

Speckle-based 3D sub-diffraction imaging of sparse samples through a multimode fiber


APL Photonics (December 2024)

Multimode fiber ruler for detecting nanometric displacements

APL Photonics (August 2022)


Abrupt X-to-O-wave structural field transition in presence of anomalous dispersion

APL Photonics (December 2024)



**Your One-Stop Shop for the
Best Brands in Optics**

- Extensive inventory with over 34,000 products available & 2,900 new products
- Fast shipping from our 9 distribution centres around the globe
- Bringing 80+ years of optical expertise to customers worldwide

 **Edmund**
optics | worldwide

[Shop Now](#)

Quantitative phase imaging with a multimode fiber

Cite as: APL Photon. 10, 046116 (2025); doi: 10.1063/5.0253648

Submitted: 18 December 2024 • Accepted: 26 March 2025 •

Published Online: 21 April 2025



Aleksandra Ivanina,^{1,2} Maxim Marshall,^{1,3}  Ksenia Abrashitova,^{1,a)} Tristan van Leeuwen,^{4,5} 
and Lyubov V. Amitonova^{1,2,b)} 

AFFILIATIONS

¹Advanced Research Center for Nanolithography (ARCNL), Science Park 106, 1098 XG, Amsterdam, The Netherlands

²Department of Physics and Astronomy, Vrije Universiteit Amsterdam, De Boelelaan 1081, 1081 HV, Amsterdam, The Netherlands

³University of Amsterdam, Science Park 908, 1098 XH, Amsterdam, The Netherlands

⁴Centrum Wiskunde & Informatica (CWI), Science Park 123, 1098 XG, Amsterdam, The Netherlands

⁵Utrecht University, Department of Mathematics, Budapestlaan 6, 3584 CD, Utrecht, The Netherlands

^{a)}Current address: Smart Photonics, High Tech Campus 37, 5656 AE, Eindhoven, The Netherlands

^{b)}Author to whom correspondence should be addressed: lamitonova@vu.nl

ABSTRACT

Label-free quantitative phase imaging is vital for optical microscopy and metrology applications. A multimode fiber stands out as a desirable platform for imaging. Here, we propose and experimentally demonstrate a non-interferometric non-iterative approach for high-speed high-resolution label-free quantitative phase imaging via a random light scattering in a multimode fiber.

© 2025 Author(s). All article content, except where otherwise noted, is licensed under a Creative Commons Attribution (CC BY) license (<https://creativecommons.org/licenses/by/4.0/>). <https://doi.org/10.1063/5.0253648>

I. INTRODUCTION

Multimode fibers (MMFs) have recently emerged as an ultimate endoscopic technology that enables high-resolution imaging at the tip of a hair-thin flexible probe.^{1,2} A wide range of imaging modalities through MMF-based endoscopes have been demonstrated, including (auto-)fluorescence,^{3–6} confocal reflectance,^{7,8} chemically-selective,⁹ super-resolution,^{10,11} and 3D^{12,13} imaging. However, even nowadays, state-of-the-art fiber-based microscopy relies on amplitude-only contrasts; to visualize “phase objects,” such as refractive index variations or matter density, quantitative phase information is required.^{14–16} As conventional detectors record only the amplitude of light, advanced approaches are needed to recover the phase. This fundamental problem stimulates the development of many techniques. Quantitative phase imaging (QPI) is a set of label-free methods to measure the optical path length delays within the sample. The problem of recovering the complex wavefront can be solved by interferometric approaches. By recording interference between an unknown field and a known reference, the incident field can be reconstructed. The spatial resolution of holographic phase microscopy can be improved by speckle field illumination.¹⁷ Holography requires extreme environmental stability and a

high-quality reference beam limiting its realizations and applications.¹⁸ A broad range of techniques that eliminate the use of a reference includes Fourier ptychography¹⁹ and differential phase contrast microscopy.²⁰ These methods reconstruct the phase shift from a relatively large sequence of intensity patterns and require iterative computationally expensive post-processing. One of the most popular non-interferometric QPI methods is Shack–Hartmann (SH) wavefront sensing.²¹ A lenslet array creates focused spots, the positions of which depend linearly on the local phase. A similar principle of using a microlens array for multiplexing the angular domain into the spatial domain is also broadly used in light-field cameras.²² However, the lenslet manufacturing parameters—total number, focal length, curvature, and diameter of lenses—limit the resolution and sensibility. Multiple solutions that utilize structurally modulated light have been proposed to overcome the limitations.^{23–26} Soldevila *et al.*²⁶ demonstrated QPI using a sequence of binary amplitude-only patterns and a single focusing lens. However, this imposes strict limits on the illumination system.

Despite all the recent progress, the development of a compact high-resolution QPI remains an important goal. Recently, a reference-free holographic image sensor, which exploits a commercial diffuser as a holographic lens, has been proposed.²⁷ Introduction

of fiber requires complex probe designs: QPI through a fiber bundle with a GRIN lens²⁸ and multicore fiber has been demonstrated.^{29,30} These methods require capturing several high-resolution images and/or complex iterative or machine learning-based reconstruction. High spatial resolution is another major challenge of QPI, especially for compact non-interferometric sensors.^{31,32} The lateral resolution of optical imaging is generally limited by the diffraction of light,

$$\mu_{\min} = k \frac{\lambda}{NA}, \quad (1)$$

where μ_{\min} is the smallest resolvable distance, λ is the wavelength of the incident radiation, and NA is the numerical aperture of the optical system. The critical parameter k is determined by the imaging modality and yields either 0.5 or 0.82 for conventional incoherent and coherent imaging, respectively. Therefore, the lateral resolution of QPI is generally determined by the $0.82\lambda/NA$ diffraction limit.^{32,33}

We propose and experimentally demonstrate non-interferometric quantitative phase imaging using random speckle illumination of an MMF. To the best of our knowledge, this is the first demonstration of QPI utilizing centroid coordinates and random complex illumination. An appealing feature is that the lateral resolution is limited by the incoherent diffraction limit of the illumination, which is 1.5 times better than the diffraction limit of conventional QPI. Moreover, we eliminate the need for a camera and rely solely on position-sensitive detection (PSD). We experimentally demonstrate quantitative phase reconstruction of a variety of phase targets with a simple noniterative algorithm.

II. MAIN PRINCIPLE

The main idea of the proposed approach is illustrated in Fig. 1(a). Coherent light coupled into an MMF gives rise to a complex speckle pattern, $B_m(x, y)e^{i\psi_m(x, y)}$. We use a set of these seemingly random patterns to sample the unknown wavefront. Each pattern illuminates the unknown sample, $A(x, y)e^{i\phi(x, y)}$, and a single lens is used to form phase-sensitive intensity distributions in the Fourier plane for transmitted or reflected light—a principle also fundamental to Shack–Hartmann sensors or light-field cameras. A position-sensitive detector in the back focal plane of the lens records the coordinates of the center of mass, (u_m, v_m) , and the total transmitted intensity, P_m . Both the amplitude and phase of the sample can be computationally recovered using the linear relationship between the local wavefront slope at the sample plane and centroid displacement in a Fourier plane.^{34,35} As we derive in Appendix A, the position of the centroid (u_m, v_m) is linked to the gradient of the phase by

$$\begin{pmatrix} u_m \\ v_m \end{pmatrix} = \frac{\lambda F}{2\pi P_m} \iint (B_m(x, y)A(x, y))^2 \nabla (\phi(x, y) + \psi_m(x, y)) dx dy, \quad (2)$$

where F is the focal distance of the lens; $A(x, y) \leq 1$ is the amplitude attenuation of the sample; $\phi(x, y)$ is the phase delay introduced by the sample; $B_m(x, y)$ is the amplitude and $\psi_m(x, y)$ is the phase of the m th speckle pattern; $P_m = \iint B_m^2(x, y)A^2(x, y) dx dy$ is the total power transmitted through the sample for each speckle pattern; and $\nabla = (\partial/\partial x, \partial/\partial y)$ is the gradient in two dimensions.

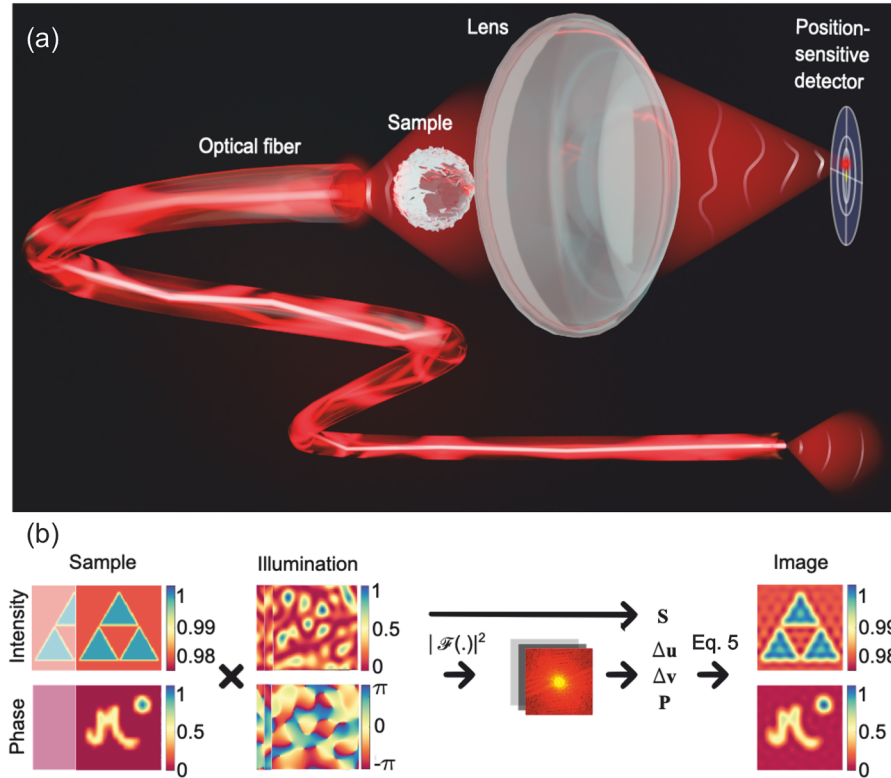


FIG. 1. (a) Schematic of the experimental setup. (b) Experimental workflow depicted through the simulation results. Complex speckle fields (second column) illuminate the unknown sample (first column). The center of mass coordinates in the Fourier plane to the “reference” sample, $\Delta u_n, \Delta v_n$, and the total transmitted power, P_m , are recorded using the position-sensitive detector. $|\mathcal{F}(\cdot)|$ denotes the Fourier transform. Matrix \mathbf{S} is measured during pre-calibration. The sample phase and amplitude are reconstructed using the proposed framework.

The main challenges of solving Eq. (2) for unknown $\phi(x, y)$ and $A(x, y)$ include the computational reconstruction of the wavefront at all points in space from “single-pixel” measurements (centroid position), demultiplexing, and the distillation of the sample field from the field of complex illumination patterns. As derived in [Appendixes B and C 1](#), the problem can be solved directly if the full calibration of the imaging system is performed and both amplitude $B_m(x, y)$ and phase $\psi_m(x, y)$ of illuminating speckle patterns are known. While this full transmission matrix pre-calibration is experimentally possible,³⁶ in real-life scenarios, it might be difficult to measure phase profiles of the speckle patterns.

We propose an elegant solution to reconstruct the unknown sample wavefront using simplified pre-calibration—only intensity maps $S_m(x, y) = B_m^2(x, y)$ of the speckle patterns. While this approach still requires pre-calibration, the recording of intensity patterns without phase stepping or external references is simpler than the full transmission matrix measurements. The proposed approach works for phase-only samples as well as for measuring (e.g., time-dependent) phase changes of a sample with a constant amplitude profile. The key is to implement a differential measurement scheme and use a set of centroid positions (u_{m0}, v_{m0}) of a reference, e.g., flat phase, sample. For continuous monitoring of phase changes of a given sample, (u_{m0}, v_{m0}) are the coordinates of the centroid position at a previous time-stamp. The gradient of the sample phase can be reconstructed without knowing the complex phase distributions of illuminating speckle patterns, as derived in [Appendix C 2](#).

The unknown amplitude and phase can be represented by vectors $\mathbf{a} \in \mathbb{R}^N$ and $\partial\phi/\partial x \equiv \phi_x \in \mathbb{R}^N$, $\partial\phi/\partial y \equiv \phi_y \in \mathbb{R}^N$, which are the squared amplitudes $A(x, y)^2$ and phase gradient $\nabla\phi(x, y)$ on a grid of N pixels. Similarly, we represent the measured relative centroid positions in the x and y directions corresponding to the M speckle patterns by $\Delta\mathbf{u} \in \mathbb{R}^M$ and $\Delta\mathbf{v} \in \mathbb{R}^M$. The unknown amplitude and phase from these measurements can be reconstructed as follows:

$$\mathbf{a} = \mathbf{S}^\dagger \mathbf{p},$$

$$\begin{pmatrix} \phi_x \\ \phi_y \end{pmatrix} = \begin{pmatrix} \mathbf{M}^\dagger & \mathbf{0} \\ \mathbf{0} & \mathbf{M}^\dagger \end{pmatrix} \begin{pmatrix} \Delta\mathbf{u} \\ \Delta\mathbf{v} \end{pmatrix}, \quad (3)$$

where

$$\mathbf{M} = \frac{\lambda F}{2\pi} \text{diag}(\mathbf{p})^{-1} \mathbf{S} \text{diag}(\mathbf{a}), \quad (4)$$

with $\mathbf{S} \in \mathbb{R}^{M \times N}$ consisting of M rows of $\text{vec}(B_m(x, y)^2)$, and $\mathbf{p} \in \mathbb{R}^M$, a vector with the total transmitted power, P_m , for each speckle pattern. The operator $\text{diag}(\cdot)$ constructs a matrix with the given vector on its diagonal, the operator $\text{vec}(\cdot)$ converts the matrix into a vector, and † denotes the Moore–Penrose pseudo-inverse.³⁷ We can explicitly compute the pseudo-inverse through the singular value decomposition (SVD) and regularize the computation by truncating small singular values. Note that in case $M < N$, the pseudo-inverse can only recover up to elements in the null-space of the matrix. The amplitude map $A(x, y)$ is reconstructed by reshaping and calculating the square root of \mathbf{a} , and the quantitative phase map

$\phi(x, y)$ is calculated by reshaping and numerically integrating ϕ_x, ϕ_y .

III. SIMULATIONS

The experimental workflow is schematically shown in [Fig. 1\(b\)](#), where we also present our simulation results. We simulate the entire procedure of phase and amplitude imaging via the proposed approach. A complex sample [$N = 92 \times 92$ pixels] is presented in [Fig. 1\(b\)](#), first column, together with a “reference” wavefront. As an illumination, a set of $M = 92 \times 92 = 8464$ fully-developed random speckle patterns with the diffraction-limited speckle size is generated. We assume the speckle patterns to be known or pre-characterized experimentally. Examples of illumination phase $\psi_m(x, y)$ and intensity $S_m(x, y)$ distributions are presented in [Fig. 1\(b\)](#), second column. The finite NA of an MMF has been simulated by using a circular coherent transfer function in the Fourier plane.³⁸ Each speckle pattern illuminates the sample or, in simulations, is multiplied by a sample complex transmission function $A(x, y)e^{i\phi(x, y)}$. The intensity distributions in the Fourier plane are measured at the back focal plane of the lens or simulated by the Fourier transform.³⁴ The total transmitted power and the centroid coordinates for each speckle illumination pattern are obtained. The procedure is repeated for the reference object with a plane phase profile. The amplitude of the sample is reconstructed using the first expression in Eq. (3), which follows a similar approach to speckle-based compressive imaging through the MMF.² Phase gradients along the x - and y -directions are computed using the second expression in Eq. (3). The spatial phase profile $\phi(x, y)$ is reconstructed by numerical integration. The results of the simulations and reconstructed amplitude and phase distributions are shown in [Fig. 1\(b\)](#) (right).

The proposed MMF-based QPI can be seen as a generalized ultra-compact version of a SH phase sensor. The spatial resolution of the SH type of sensors is limited by the lenslet size³⁹ or a pattern aperture size,²⁶ which in our case is equal to the average speckle size of $0.5\lambda/\text{NA}$. Therefore, the resolution of MMF-based QPI is expected to be higher than the resolution of conventional, e.g., holographic, coherent phase imaging techniques, which are limited by $0.82\lambda/\text{NA}$. To characterize the lateral resolution of the proposed approach, we simulate imaging of phase-only samples consisting of two phase objects separated by different distances: λ/NA , $0.76\lambda/\text{NA}$, and $0.5\lambda/\text{NA}$, as depicted in [Figs. 2\(a\), 2\(f\), and 2\(k\)](#), respectively.

To simulate conventional coherent diffraction-limited imaging without the loss of generality, we assume that the phase sample is illuminated with a plane wave and account for diffraction effects by applying the low-pass circular coherent transfer function with the cutoff frequency NA/λ in the Fourier plane. The procedure is detailed in [supplementary material 2](#) and follows the standard coherent imaging formulation described by Goodman.⁴⁰ The MMF-based QPI has been simulated, as described above [see [Fig. 1\(b\)](#)], using a set of $92 \times 92 = 8464$ fully-developed random speckle patterns. We ensure diffraction-limited illumination by cutting high spatial frequencies of simulated speckle patterns in the Fourier plane. The results are presented in [Figs. 2\(b\), 2\(g\), and 2\(l\)](#) for conventional phase imaging and in [Figs. 2\(c\), 2\(h\), and 2\(m\)](#) for the proposed MMF-based QPI. The horizontal cross sections along the centers of peaks are shown in [Figs. 2\(d\), 2\(i\), and 2\(n\)](#) by the green solid line for

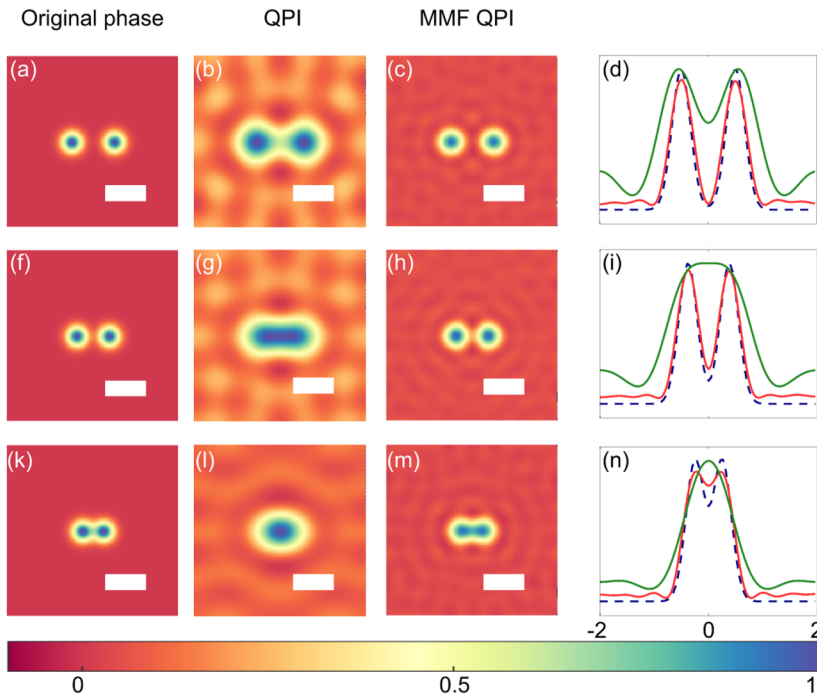


FIG. 2. Simulation results. [(a), (f), and (k)] Phase samples with distances between the dots of λ/NA (a), $0.76\lambda/NA$ (f), and $0.5\lambda/NA$ (k). Imaging results for conventional coherent imaging [(b), (g), and (l)] and proposed MMF imaging [(c), (h), and (m)]. Scale bars are $0.82\lambda/NA$. [(d), (i), and (n)] Horizontal cross sections along the peaks for the ground-truth phase (blue dashed lines), conventional imaging (green solid lines), and MMF imaging (red solid lines). The x axis is normalized to λ/NA .

the conventional and by the red solid line for the proposed approach, respectively. The ground truth is shown by the blue dashed line. As expected, the phase structures are distinguishable in Fig. 2(b) and not resolved in Figs. 2(g) and 2(l), where the feature size is smaller than $0.82\lambda/NA$. In contrast, the proposed speckle-based QPI allows us to resolve peaks at shorter distances, as can be seen in Figs. 2(h) and 2(m), up to a limit of $0.5\lambda/NA$. Our simulations confirm that the proposed workflow can be used for MMF-based QPI.

IV. EXPERIMENTAL RESULTS

We experimentally demonstrate the MMF-based QPI using a standard MMF (Thorlabs, FG050LGA) with $NA_{\text{fiber}} = 0.22$, a core diameter of $50\ \mu\text{m}$, and a length of about 20 cm, which is illuminated by a coherent laser beam with a wavelength $\lambda = 640\ \text{nm}$. To generate various speckle patterns, we scan the input facet with a focused laser beam on a circular uniform grid by displaying different amplitude gratings on the digital micromirror device, DMD (ViALUX, V9001VIS; 2560×1600 micromirrors with $7.6\ \mu\text{m}$ pixel pitch). The DMD is located in the Fourier plane of the input objective (Olympus Plan Achromat; $20\times$, $WD = 1.2\ \text{mm}$, $NA = 0.4$, $f_{\text{objl}} = 9\ \text{mm}$). The spatial frequency of the projected grating was sampled uniformly $[k_x, k_y] = -k_0 \dots k_0$ with 20 steps, which results in up to 400 incident patterns.

As a versatile re-configurable phase sample, we use a liquid crystal spatial light modulator, SLM, (Meadowlark Optics, E19x12-350-850-HDM8; 60 Hz frame rate, 1920×1200 , pxl size $8\ \mu\text{m}$). Speckle patterns from the MMF output are magnified $63\times$ to match the screen size of the SML. As a result, the illumination NA is $NA_{\text{fiber}}/63 = 3.5 \cdot 10^{-3}$. The field of view is restricted to

$780 \times 780\ \mu\text{m}^2$ or 90×90 SLM pixels using a $500\ \mu\text{m}$ square pinhole PH2 (Thorlabs, S500QK) in an intermediate image plane.

The intensity distributions of the speckle patterns, $S_m(x, y) = B_m(x, y)^2$, are recorded using a CMOS camera (IDS, 118 fps, 10-bits, exposure time 0.05 ms) during the pre-calibration step that is taking less than 4 s for 20×20 patterns. In addition, about 2 sec was required to transfer data to the SSD. Images are down-scaled to $N = 120 \times 120$ pixels. Therefore, the size of matrix S in our experiments is $M \times 14\,400$. The examples of illumination patterns are presented in Fig. 3(a). By investigating the averaged frequency content of the patterns, as presented in Fig. 3(b), we confirm that the average speckle intensity size is $0.5\lambda/NA$. The diffraction limit, together with the limited field-of-view, puts a threshold on the total number of uncorrelated speckle patterns. Our experimental configuration is expected to generate ~ 100 independent speckle patterns. To estimate the number of independent speckle patterns, we calculate the rank of the experimentally measured matrix S by a singular value decomposition. The singular values are presented in Fig. 3(c), and the rank of S matches with the number of independent speckle patterns. We test the alignments of the setup by imaging simple phase samples consisting of linear phase gradients in 2D. The detailed setup and alignment experiments are discussed in [supplementary material 1](#).

In the next set of experiments, we image different Gaussian phase distributions projected on the SLM. As an illumination, $M = 200$ random speckle patterns on the output of an MMF have been used. The intensity distribution of each speckle pattern $S_m(x, y)$ and the corresponding centroid coordinates for the flat phase profile, u_{m0}, v_{m0} , have been measured during pre-calibration. In the imaging step, the same set of speckle patterns has been used to illuminate the phase sample projected on the SLM, and the total power and

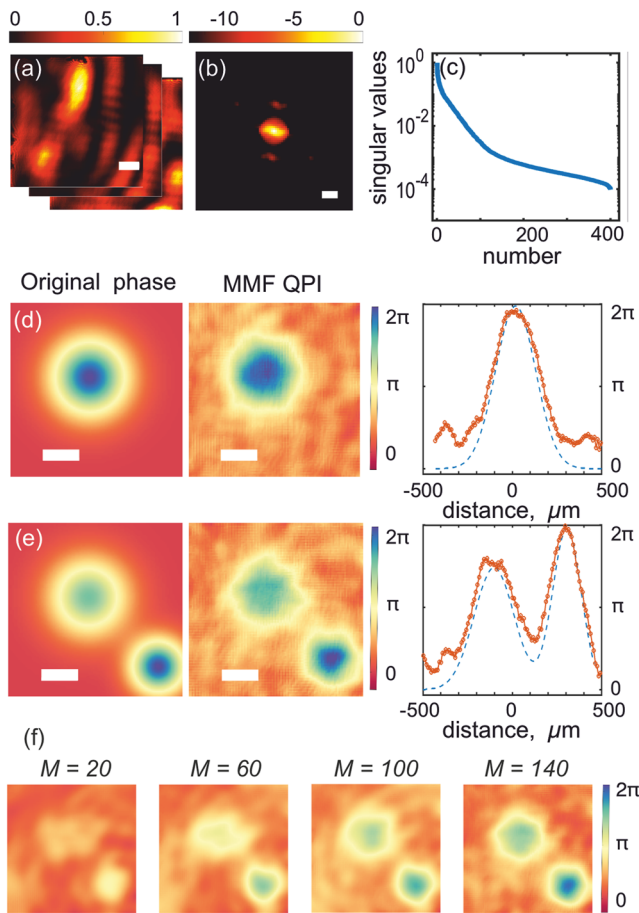


FIG. 3. Experimental results. (a) Speckle patterns generated by the MMF, $S_m(x, y)$. The scale bar is $0.5\lambda/\text{NA} \approx 92 \mu\text{m}$. (b) Zoomed-in average power spectrum density of the speckle patterns. The scale bar is $2\text{NA}/\lambda$. (c) Singular values of \mathbf{S} plotted in the descending order. [(d) and (e)] MMF-based phase imaging results: phase patterns on the SLM (left), experimentally measured and reconstructed phase (middle), and the cross sections along the center of the peaks (right) of the original patterns (blue dashed line) and their images (orange solid line). The scale bars are $0.82\lambda/\text{NA} = 150 \mu\text{m}$. (f) Imaging quality as a function of the number of illumination patterns, M , for the sample presented in (e).

the centroid coordinates have been recorded. Then, $\Delta u = u_m - u_{m0}$ and $\Delta v = v_m - v_{m0}$ have been calculated. The simplified version of Eq. (3), where $A = 1$, has been used to calculate phase gradients,

$$\nabla\phi = \frac{2\pi}{\lambda F} \mathbf{S}^\dagger \text{diag}(\mathbf{P}) \begin{pmatrix} \Delta \mathbf{u} \\ \Delta \mathbf{v} \end{pmatrix}. \quad (5)$$

Resulting $\nabla\phi_x$ and $\nabla\phi_y$ have been reshaped to 2D matrices of 120×120 pixels each. Phase has been calculated using inverse (integrated) gradient MATLAB code.

The reconstruction results are presented in Figs. 3(d) and 3(e). We see an excellent quantitative match between the reconstructed images and the original phase patterns. The cross section along the centers of Gaussian peaks of the projected patterns (blue dashed

lines) and phase images (orange lines) agrees. To investigate how the image quality scales with the number of speckle illumination patterns, we performed phase reconstruction using various sets of illumination patterns. The experimental results for $M = 20$, $M = 60$, $M = 100$, and $M = 140$ speckle patterns are shown in Fig. 3(f) from left to right. Accurate shapes begin to emerge with M as small as 60 patterns, although the image still exhibits strong noise and low contrast. A clear improvement is observed with larger values of M . For $M = 140$, the image is already quite good with a relatively smooth background, while for $M = 200$, the experimentally measured images contain a grid-like structure and an oscillatory background. This can be explained by several main factors, apart from evident experimental noise. The reconstruction algorithm uses hard thresholding of singular values, which can be seen as a generalization of Fourier low-pass filtering. This kind of background is fundamental to coherent imaging techniques and can also be seen in simulated noise-free images both for conventional and proposed approaches (Fig. 2). In addition, matrix \mathbf{S} is recorded in reflection from the SLM, which results in the superposition of the SLM pixels with the incident speckle patterns. The periodic pixel boundaries are becoming visible in the final high-resolution images.

In the third set of experiments, we image different complex phase distributions using $M = 400$ speckle patterns generated in an MMF, center-of-mass position detection scheme, and amplitude-only pre-calibration approach. The phase imaging results for complex phase samples representing letter “O” [Fig. 4(a)], university logo “VU” [Fig. 4(b)], and digit “9” [Fig. 4(c)] are presented in Figs. 4(d)–4(f), respectively.

Finally, to experimentally investigate the resolution limits of the proposed MMF QPI, we image the sample consisting of two Gaussian phase profiles [see Fig. 4(g), bottom] at a close distance of $92 \mu\text{m}$, which matches the theoretical resolution limit of the proposed MMF-based QPI, calculated as $0.5\lambda/\text{NA}$. The experimental results are presented in Fig. 4(g), top. The cross sections along the peaks shown in Fig. 4(h) demonstrate the excellent agreement between the original phase sample (blue dashed line) and the reconstructed image (red solid line), confirming the theoretically predicted resolution enhancement.

To summarize, we propose and experimentally demonstrate MMF QPI based on random complex speckle illumination and center-of-mass position detection. We have developed the necessary mathematical framework, conducted simulations, and completed proof-of-principle reflection mode experimental validation. The proposed approach can be generalized to arbitrary complex patterns and further utilized in various imaging configurations. The simulations and experimental results reveal about 1.5 times resolution enhancement compared to conventional coherent imaging. Note that the proposed approach does not require reference illumination, iterative reconstruction, any additional assumptions, or free variables. The spatial resolution and imaging speed can be further improved by advanced computational approaches, which take advantage of prior knowledge and regularization.

While the research on the ultimate phase sensitivity and maximum imaging speed lies beyond the scope of this proof-of-principle study, we outline and discuss the main timing constraints. The camera is only required for the pre-calibration step, which, while relatively time-consuming, is performed once before the imaging experiments. During phase imaging, only the center-of-mass

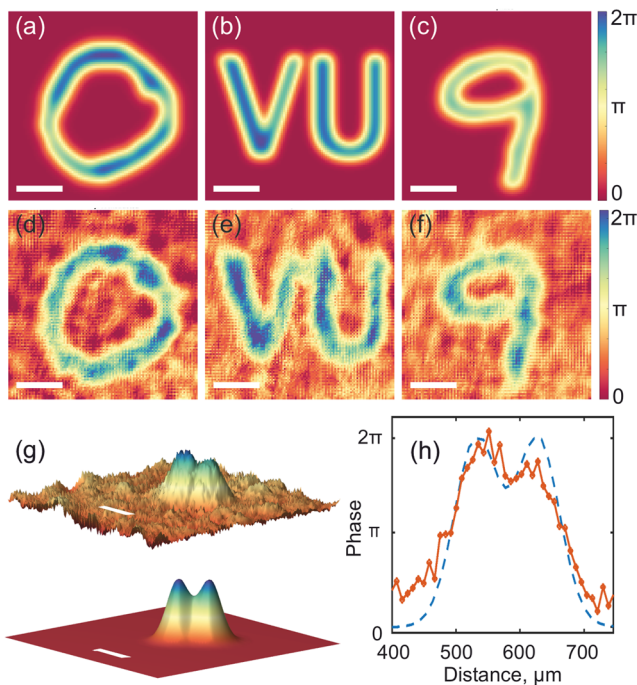


FIG. 4. MMF-based QPI of complex phase targets. [(a)–(c)] Sample phase patterns projected onto the SLM. [(d)–(f)] Experimentally measured phase patterns representing the letter “O” (d), the university logo “VU” (e), and digit “9” (f). [(g) and (h)] Experimental demonstration of high spatial resolution: (g, top) image of a phase pattern consisting of two Gaussian profiles at a close distance of $0.5\lambda/\text{NA}$ and (g, bottom) the original SLM pattern. The scale bars are $0.82\lambda/\text{NA} = 150\ \mu\text{m}$. (h) Cross sections along the centers of Gaussian peaks for the SLM pattern (the blue dashed line) and MMF-based image (the orange line).

position needs to be detected, which can be achieved using a high-speed PSD. Consequently, the imaging speed is fundamentally limited by the scanning rate and the total number of measurements. Commercial DMDs can provide a scanning rate of up to 22 kHz. Our experiments show that for the given FOV, 400 measurements and an exposure time of 0.05 ms lead to a good phase reconstruction. Thus, the proposed approach has the potential to operate at video-rate speeds, reaching 50 f/s. As it does not require iterative optimization, the computational run-time does not limit the imaging speed. The most time-consuming computational step is the matrix inversion [S^\dagger in Eq. (5)], which can be pre-computed in advance as a part of the pre-calibration procedure. Therefore, our approach offers relatively high-speed performance compared to other scanning techniques (e.g., ptychography), while single-shot interferometric methods operating at camera frame rates (such as off-axis holography) are inherently faster.

Although we rely on a precise calibration of an MMF, calibration does not require interferometric measurements and is therefore much simpler than measuring the full transmission matrix of an MMF. Our experiments show that under standard laboratory conditions, the calibration remains stable for over 90 minutes (see the [supplementary material](#), Fig. S2). Furthermore, sensitivity to bending can be mitigated using fiber modeling approach⁴¹ or by advanced

multicore-multimode fibers⁴² and swept-source imaging,⁴³ all of which are fully compatible with the proposed MMF QPI. The MMF-based noniterative QPI paves the way toward high-speed phase sensors with many applications in life science and the semiconductor industry.

SUPPLEMENTARY MATERIAL

The [supplementary material](#) details the experimental setup, alignment, stability, and diffraction limit analysis of the system, along with simulations validating its theoretical resolution limit using coherent diffraction theory.

ACKNOWLEDGMENTS

This work was conducted at the Advanced Research Center for Nanolithography, a public-private partnership between the University of Amsterdam, Vrije Universiteit Amsterdam, University of Groningen, the Netherlands Organization for Scientific Research (NWO), and the semiconductor equipment manufacturer ASML. We thank Mara Niamh Cerise van der Meulen (UvA) for her assistance in derivations of Fourier transform theorems and fruitful discussions. We thank Marco Seynen (AMOLF) and Dr. Stefan Lehmann (ARCNL) for their technical assistance.

AUTHOR DECLARATIONS

Conflict of Interest

The authors have no conflicts to disclose.

Author Contributions

A.I. and M.M. contributed equally to this work.

Aleksandra Ivanina: Data curation (equal); Formal analysis (equal); Investigation (equal); Methodology (supporting); Writing – original draft (supporting); Writing – review & editing (supporting). **Maxim Marshall:** Data curation (equal); Formal analysis (equal); Investigation (equal); Methodology (supporting); Writing – original draft (supporting); Writing – review & editing (supporting). **Ksenia Abrashitova:** Conceptualization (supporting); Data curation (equal); Formal analysis (equal); Investigation (equal); Methodology (equal); Writing – original draft (equal); Writing – review & editing (equal). **Tristan van Leeuwen:** Conceptualization (supporting); Data curation (equal); Formal analysis (equal); Methodology (equal); Supervision (supporting); Writing – original draft (supporting); Writing – review & editing (supporting). **Lyubov V. Amitonova:** Conceptualization (lead); Formal analysis (equal); Funding acquisition (lead); Investigation (supporting); Methodology (equal); Supervision (lead); Writing – original draft (equal); Writing – review & editing (equal).

DATA AVAILABILITY

The data that support the findings of this study are available from the corresponding author upon reasonable request.

APPENDIX A: THEORETICAL DERIVATIONS

1. Fourier transform theorems

Some theorems regarding the Fourier transform are used in the derivations in this paper; they are presented here with proof. The Fourier transform of a square-integrable function $f: \mathbb{R}^2 \rightarrow \mathbb{C}$ is written as $\widehat{f} = \mathcal{F}\{f\}$ and is defined by

$$\mathcal{F}\{f\}(\mathbf{x}) := \int_{\mathbb{R}^2} \widehat{f}(\xi) e^{2\pi i \xi \cdot \mathbf{x}} d\xi. \quad (\text{A1})$$

Its inverse is given by

$$\mathcal{F}^{-1}\{\widehat{f}\}(\xi) := \int_{\mathbb{R}^2} f(\mathbf{x}) e^{-2\pi i \xi \cdot \mathbf{x}} d\mathbf{x}. \quad (\text{A2})$$

Lemma 1. For a square-integrable and sufficiently smooth function $f: \mathbb{R}^2 \rightarrow \mathbb{C}$, we have

$$2\pi i \int \xi \widehat{f}(\xi)^2 d\xi = \int \overline{f(\mathbf{x})} \nabla f(\mathbf{x}) d\mathbf{x}. \quad (\text{A3})$$

Proof. Express

$$f(\mathbf{x}) = \int \widehat{f}(\xi) e^{-2\pi i \xi \cdot \mathbf{x}} d\xi,$$

$$\nabla f(\mathbf{x}) = 2\pi i \int \xi \widehat{f}(\xi) e^{-2\pi i \xi \cdot \mathbf{x}} d\xi,$$

which yield

$$\int \overline{f(\mathbf{x})} \nabla f(\mathbf{x}) d\mathbf{x} = 2\pi i \iiint \xi \widehat{f}(\xi) \widehat{f}(\xi') e^{2\pi i \xi \cdot (\xi - \xi')} d\mathbf{x} d\xi d\xi'.$$

Using that $\int e^{2\pi i (\xi - \xi') \cdot \mathbf{x}} d\mathbf{x} = \delta(\xi - \xi')$, we get the desired result. ■

Theorem 1. For a square-integrable and sufficiently smooth function $f: \mathbb{R}^2 \rightarrow \mathbb{C}$, we have

$$\int_{\mathbb{R}^2} |f(\mathbf{x})|^2 \nabla \theta(\mathbf{x}) d\mathbf{x} = 2\pi \int_{\mathbb{R}^2} \xi \widehat{f}(\xi)^2 d\xi, \quad (\text{A4})$$

where $\theta = \arg(f)$ denotes the phase of f .

Proof. Express $f(\mathbf{x}) = a(\mathbf{x}) e^{i\theta(\mathbf{x})}$ and apply Lemma 1,

$$\begin{aligned} 2\pi \int_{\mathbb{R}^2} \xi \widehat{f}(\xi)^2 d\xi &= -i \int_{\mathbb{R}^2} \overline{f(\mathbf{x})} (\nabla a(\mathbf{x}) + ia(\mathbf{x}) \nabla \theta(\mathbf{x})) e^{i\theta(\mathbf{x})} d\mathbf{x} \\ &= \int_{\mathbb{R}^2} |f(\mathbf{x})|^2 \nabla \theta(\mathbf{x}) d\mathbf{x} - i \int_{\mathbb{R}^2} a(\mathbf{x}) \nabla a(\mathbf{x}) d\mathbf{x}. \end{aligned} \quad (\text{A5})$$

The left-hand side is real-valued, as is the first term on the right-hand side. Since a is strictly real-valued, consequently $\int a(\mathbf{x}) \nabla a(\mathbf{x}) d\mathbf{x} = 0$. ■

2. Main equation

Suppose we illuminate the ultimately thin sample with various illumination patterns. We analyze corresponding fields in the

Fourier plane (far field) of a lens with the focal distance F . The field of the m -th illumination pattern as it arrives at the sample plane is given by

$$E_m^{\text{inc}} = B_m(x, y) e^{i\psi_m(x, y)}, \quad (\text{A6})$$

where $B_m(x, y)$ is the amplitude of the incident field, $\psi_m(x, y)$ is the phase of the incident illumination, and x and y are coordinates in a sample plane. The incident illumination interacts with the sample, subsequently getting the amplitude and the phase modulation. The field just after the ultimately thin sample is given by

$$E_m^{\text{sample}}(x, y) = \gamma(x, y) E_m^{\text{inc}}(x, y) = A(x, y) B_m(x, y) e^{i(\phi(x, y) + \psi_m(x, y))}, \quad (\text{A7})$$

where $\gamma(x, y)$ is the complex transmission function of the sample, $A(x, y)$ is the amplitude transmission function of the sample, and $\phi(x, y)$ is the phase delay that the sample induces. According to the Fraunhofer diffraction theory, the field in the back focal plane of the thin lens is proportional to the Fourier transform of the sample field,⁴⁰

$$E_m^{\text{out}}(u, v) = \frac{e^{iC}}{\lambda F} \mathcal{F}\{E_m^{\text{sample}}\}(u/(\lambda F), v/(\lambda F)), \quad (\text{A8})$$

where C is a coordinate-dependent phase factor, $E_m^{\text{out}}(u, v)$ is the field in the back focal plane of the lens, u and v are the coordinates in the back focal plane of the lens, λ is the wavelength of light, and F is the lens focal distance.

We now apply Theorem 1 with $f(\mathbf{x}) = E_m^{\text{sample}}(x, y)$ taking into account the relation stated in Eq. (A8) to produce a key result of this derivation, a relation between the measured centroid position (u, v) and the unknown phase gradient $\nabla \phi(x, y)$,

$$\begin{aligned} \frac{2\pi}{\lambda F} \iint \left(\frac{u}{v} \right) \cdot |E_m^{\text{out}}(u, v)|^2 du dv &= \iint |E_m^{\text{sample}}(x, y)|^2 \nabla(\phi(x, y) \\ &\quad + \psi_m(x, y)) dx dy. \end{aligned} \quad (\text{A9})$$

We note that the left-hand side of Eq. (A9) corresponds to the spectral power centroid of the sample field, a measurable quantity that is given by

$$\left(\frac{u_m}{v_m} \right) = \frac{1}{P_m} \iint \left(\frac{u}{v} \right) \cdot |E_m^{\text{out}}(u, v)|^2 du dv, \quad (\text{A10})$$

where P_m is the total transmitted power expressed by the following equation:

$$\begin{aligned} P_m &= \iint |E_m^{\text{out}}(u, v)|^2 du dv = \iint |E_m^{\text{sample}}(x, y)|^2 dx dy \\ &= \iint |E_m^{\text{inc}}(x, y) \gamma(x, y)|^2 dx dy = \iint B_m(x, y)^2 A(x, y)^2 dx dy. \end{aligned} \quad (\text{A11})$$

Eq. (A11) links the unknown intensity transmission function of the sample $A^2(x, y)$ with the calibrated intensity distribution of incident patterns $B_m^2(x, y)$ and the measured total transmitted power P_m .

By multiplying the left and the right sides of Eq. (A9) by the factor $\lambda F / (2\pi P_m)$ and taking into account Eq. (A10), we can rewrite Eq. (A9) in the following form:

$$\begin{pmatrix} u_m \\ v_m \end{pmatrix} = \frac{\lambda F}{2\pi P_m} \iint B_m(x, y)^2 A(x, y)^2 \nabla(\phi(x, y) + \psi_m(x, y)) dx dy. \quad (\text{A12})$$

The left side of Eq. (A12) is the centroid position in the back focal plane of the lens, the integrated quantity that can be measured with the position-sensitive detector. The right-hand side of Eq. (A12) is a functional of the unknown phase gradient of the sample $\phi(x, y)$, the unknown intensity transmission function of the sample $A^2(x, y)$, the known (pre-calibrated) phase gradient of the illumination pattern, $\psi_m(x, y)$, the known (pre-calibrated) intensity distribution of the incident illumination $B_m^2(x, y)$, and the total optical power P_m .

APPENDIX B: SPECIAL CASES

In this section, we consider Eq. (A12) for three special cases of illumination patterns and samples: the first case assumes complex illumination patterns and purely phase sample, the second case assumes complex illumination patterns and phase and amplitude sample, and the third case assumes binary amplitude modulation of illumination patterns and purely phase sample.

1. Complex illumination of a phase-only sample

If the illumination patterns $S_m(x, y)$ are complex-valued and the sample does not induce amplitude modulation of the incident patterns $A(x, y) \equiv 1$ for $\forall x, y$, we can write

$$\begin{pmatrix} u_m \\ v_m \end{pmatrix} = \frac{\lambda F}{2\pi P_m} \iint B_m(x, y)^2 \nabla(\phi(x, y) + \psi_m(x, y)) dx dy. \quad (\text{B1})$$

We can recognize that the very last term of the right part of the equation is the spectral power centroid position in the absence of a sample,

$$\begin{pmatrix} u_{m0} \\ v_{m0} \end{pmatrix} = \frac{\lambda F}{2\pi P_m} \iint B_m(x, y)^2 \nabla \psi_m(x, y) dx dy. \quad (\text{B2})$$

Therefore, we can rewrite Eq. (B1),

$$\begin{pmatrix} \Delta u_m \\ \Delta v_m \end{pmatrix} = \begin{pmatrix} u_m - u_{m0} \\ v_m - v_{m0} \end{pmatrix} = \frac{\lambda F}{2\pi P_m} \iint B_m(x, y)^2 \nabla \phi(x, y) dx dy, \quad (\text{B3})$$

where $(\Delta u_m, \Delta v_m)$ is the shift of the power centroid position induced by the phase modulation of the sample. The introduction of $\begin{pmatrix} u_{m0} \\ v_{m0} \end{pmatrix}$ allows us to eliminate the necessity of the complicated interferometric measurements of the phase of the incident patterns $\psi_m(x, y)$.

2. Complex illumination of a phase and amplitude sample

Here, we consider the case where the sample is not a purely phase object but modulates both the amplitude and phase of the incident radiation. To extract the spatial phase profile of the sample according to Eq. (A12), we need to know the phase and intensity profiles of the incident patterns. As the amplitude modulation of the sample, $A(x, y)$, can be calculated from the total transmitted power measurements P_m and the illumination patterns can be fully characterized via pre-calibration, we can define the functionals α and β as

$$\begin{pmatrix} \alpha \\ \beta \end{pmatrix} = \frac{\lambda F}{2\pi P_m} \iint (A(x, y) B_m(x, y))^2 \nabla \psi_m(x, y) dx dy, \quad (\text{B4})$$

and rewrite Eq. (A12) as

$$\begin{pmatrix} u_m - \alpha \\ v_m - \beta \end{pmatrix} = \frac{\lambda F}{2\pi P_m} \iint (A(x, y) B_m(x, y))^2 \nabla \phi(x, y) dx dy. \quad (\text{B5})$$

We are interested not only in the phase map of the sample but in the phase map changes over time. Assuming that the amplitude transmission function of the sample does not change, we can write down the set of equations similarly to the pure phase sample case, Eq. (B3). The calculation of the sample phase map does not require measuring phase distributions of the illumination patterns,

$$\begin{pmatrix} u_{m0} \\ v_{m0} \end{pmatrix} = \frac{\lambda F}{2\pi P_m} \iint (A(x, y) B_m(x, y))^2 \nabla \times [\psi_m(x, y) + \phi_{i1}(x, y)] dx dy, \quad (\text{B6})$$

$$\begin{pmatrix} \Delta u_m \\ \Delta v_m \end{pmatrix} = \begin{pmatrix} u_m - u_{m0} \\ v_m - v_{m0} \end{pmatrix} = \frac{\lambda F}{2\pi P_m} \iint B_m(x, y)^2 A(x, y)^2 \nabla \phi_{i2}(x, y) dx dy, \quad (\text{B7})$$

where $(\Delta u_m, \Delta v_m)$ is the shift of the power centroid position induced by the phase difference at the different moments in time.

3. Binary illumination of a phase-only sample

To compare the equations derived in the current article with the equations reported previously in the literature in Ref. 26, we also rewrite Eq. (A12) for the simplified case of ideal binary patterns and a pure phase sample. Taking into account that in this case the incident illumination patterns have planar wavefronts $\nabla \psi_m(x, y) \equiv 0$, the sample does not introduce amplitude modulation $A(x, y) \equiv 1$, and the patterns are binary, $B_m^2(x, y) = B_m(x, y) = 1$ for $\forall x, y \in \mathcal{A}_m$ and $B_m^2(x, y) = B_m(x, y) = 0$ for $\forall x, y \notin \mathcal{A}_m$, we get

$$\begin{pmatrix} u_m \\ v_m \end{pmatrix} = \frac{\lambda F}{2\pi P_m} \iint_{\mathcal{A}_m} \nabla \phi(x, y) dx dy, \quad (\text{B8})$$

where \mathcal{A}_m is the region of the sample where the m th illumination pattern is non-zero and $P_m = \iint_{\mathcal{A}_m} 1 dx dy$ is the area corresponding

to that region. This result for the ideal simplified case is identical to that obtained in Ref. 26.

APPENDIX C: EQUATIONS IN A MATRIX FORM

Here, we discuss the proposed procedure to solve the equations and reconstruct the unknown phase of the sample by using the discretized matrix form. We assume that the image plane and Fourier plane fields are sampled on a $N_1 \times N_2$ uniform grid with $N = N_1 \cdot N_2$ grid points, where (u', v') and (x', y') are the grid coordinates in the Fourier and the sample plane, respectively, and $\varepsilon \times \varepsilon$ is the pixel size in the sample plane. The discrete versions of the incident illumination and the sample can be introduced as the values averaged over a respective pixel area $B_m[x', y'] \exp(\psi_m[x', y'])$ and $A[x', y'] \exp(\phi[x', y'])$. Using these notations and substituting continuous integrals with discrete sums, we can transform the derived integral equations to the systems of linear equations.

1. General case

First, we derive the equation to reconstruct the amplitude transmission function of the sample $A[x', y']$ from the total transmitted power P_m . We can write the discretized version of Eq. (A11) as

$$P_m = \sum_{x'} \sum_{y'} S_m[x', y'] A[x', y']^2 \varepsilon^2, \quad (C1)$$

where $S_m[x', y'] = B_m^2[x', y']$ is the discretized power distribution of incident speckle patterns.

We introduce vector $\mathbf{p} \in \mathbb{R}^M$ representing the total transmitted power for each speckle illumination pattern, with P_m being the m^{th} element, the matrix $\mathbf{S} \in \mathbb{R}^{M \times N}$ containing the power distributions of the speckle patterns, and the vector $\mathbf{a} \in \mathbb{R}^N$ representing the intensity transmission function of the sample with elements $A[x_n, y_n]^2$. Using these notations, we rewrite the set of Eq. (C1) in the matrix form,

$$\mathbf{p} = \mathbf{S}\mathbf{a}, \quad (C2)$$

and its solution using the Moore–Penrose pseudoinverse,

$$\mathbf{a} = \mathbf{S}^\dagger \mathbf{p}, \quad (C3)$$

getting the first equation of the set of Eq. (3) of the main article. The amplitude transmission $A[x', y']$ is reconstructed by the transformation of the vector \mathbf{a} into the 2D map $A^2[x', y']$ and taking the square root. We note that the solution to Eq. (C2) may neither exist (e.g., when $M > N$) nor be unique (e.g., when $M < N$ as often in experiments). The pseudo-inverse [cf. (C3)] provides a minimum-norm least-squares solution in these cases. In particular, in experimentally relevant settings, we often have $M < N$ and we retrieve \mathbf{a} up to components in the null-space of \mathbf{S} . We can explicitly compute the pseudo-inverse through the singular value decomposition (SVD) and regularize the computation by truncating small singular values.

Second, we derive the equation to reconstruct the phase map of the sample $\phi[x', y']$. We use the discretized version of Eq. (B5),

$$\begin{pmatrix} u_m - \alpha_m \\ v_m - \beta_m \end{pmatrix} = \frac{\lambda F}{2\pi} \frac{1}{P_m} \sum_{x'} \sum_{y'} S_m[x', y'] (A[x', y'])^2 \nabla(\phi[x', y']) \varepsilon^2. \quad (C4)$$

Introducing the vectors $\mathbf{u} \in \mathbb{R}^M$ and $\mathbf{v} \in \mathbb{R}^M$ representing the x - and y -coordinates of the centroid in the Fourier plane, vectors $\boldsymbol{\alpha} \in \mathbb{R}^M$ and $\boldsymbol{\beta} \in \mathbb{R}^M$ representing the functionals of the incident speckle patterns, and ϕ_x and ϕ_y denoting the derivatives in the x and y directions of ϕ on the grid, Eq. (C4) can be written as

$$\begin{pmatrix} \mathbf{u} - \boldsymbol{\alpha} \\ \mathbf{v} - \boldsymbol{\beta} \end{pmatrix} = \begin{pmatrix} \mathbf{M} & \mathbf{0} \\ \mathbf{0} & \mathbf{M} \end{pmatrix} \begin{pmatrix} \phi_x \\ \phi_y \end{pmatrix}, \quad (C5)$$

with

$$\mathbf{M} = \frac{\lambda F}{2\pi} \text{diag}(\mathbf{p})^{-1} \mathbf{S} \text{diag}(\mathbf{a}). \quad (C6)$$

With this, the unknown quantities ϕ_x, ϕ_y can be calculated by applying \mathbf{M}^\dagger to $\mathbf{u} - \boldsymbol{\alpha}$ and $\mathbf{v} - \boldsymbol{\beta}$. The phase ϕ can be computed from ϕ_x, ϕ_y by numerical integration.

2. Differential scheme

Similarly, we write the matrix form of Eq. (B6) as

$$\begin{pmatrix} \Delta \mathbf{u} \\ \Delta \mathbf{v} \end{pmatrix} = \begin{pmatrix} \mathbf{M} & \mathbf{0} \\ \mathbf{0} & \mathbf{M} \end{pmatrix} \begin{pmatrix} \phi_x \\ \phi_y \end{pmatrix}, \quad (C7)$$

where $\Delta \mathbf{u}$ and $\Delta \mathbf{v}$ are vectors with the elements $\Delta u_m = u_m - u_{m0}$ and $\Delta v_m = v_m - v_{m0}$ representing the relative shift of the centroid position with respect to the reference point in x - and y -directions, respectively. In this case, the unknown phase gradients can be calculated as

$$\begin{pmatrix} \phi_x \\ \phi_y \end{pmatrix} = \begin{pmatrix} \mathbf{M}^\dagger & \mathbf{0} \\ \mathbf{0} & \mathbf{M}^\dagger \end{pmatrix} \begin{pmatrix} \Delta \mathbf{u} \\ \Delta \mathbf{v} \end{pmatrix}, \quad (C8)$$

which is the second equation in the set of Eq. (3) of the main article.

REFERENCES

- ¹H. Cao, T. Čižmar, S. Turtaev, T. Tyc, and S. Rotter, "Controlling light propagation in multimode fibers for imaging, spectroscopy, and beyond," *Adv. Opt. Photonics* **15**, 524–612 (2023).
- ²L. V. Amitonova, "Multimode fiber endoscopes for computational brain imaging," *Neurophotonics* **11**, S11509 (2024).
- ³T. Čižmar and K. Dholakia, "Shaping the light transmission through a multimode optical fibre: Complex transformation analysis and applications in biophotonics," *Opt. Express* **19**, 18871–18884 (2011).
- ⁴S. Ohayon, A. Caravaca-Aguirre, R. Piastun, and J. J. DiCarlo, "Minimally invasive multimode optical fiber microendoscope for deep brain fluorescence imaging," *Biomed. Opt. Express* **9**, 1492–1509 (2018).
- ⁵B. Lochocki, M. V. Verweg, J. J. M. Hoozemans, J. F. de Boer, and L. V. Amitonova, "Epi-fluorescence imaging of the human brain through a multimode fiber," *APL Photonics* **7**, 071301 (2022).
- ⁶M. Stibůrek, P. Ondráčková, T. Tučková, S. Turtaev, M. Šiler, T. Pikálek, P. Jákl, A. Gomes, J. Krejčí, P. Kolbábková, H. Uhlířová, and T. Čižmar, "110 μm thin endo-microscope for deep-brain in vivo observations of neuronal connectivity, activity and blood flow dynamics," *Nat. Commun.* **14**, 1897 (2023).

- ⁷D. Loterie, S. A. Goorden, D. Psaltis, and C. Moser, "Confocal microscopy through a multimode fiber using optical correlation," *Opt. Lett.* **40**, 5754–5757 (2015).
- ⁸S.-Y. Lee, V. J. Parot, B. E. Bouma, and M. Villiger, "Confocal 3D reflectance imaging through multimode fiber without wavefront shaping," *Optica* **9**, 112–120 (2022).
- ⁹J. Trägårdh, T. Pikálek, M. Šerý, T. Meyer, J. Popp, and T. Čížmár, "Label-free cars microscopy through a multimode fiber endoscope," *Opt. Express* **27**, 30055–30066 (2019).
- ¹⁰L. V. Amitonova and J. F. de Boer, "Endo-microscopy beyond the abbe and Nyquist limits," *Light: Sci. Appl.* **9**, 81 (2020).
- ¹¹K. Abrashitova and L. V. Amitonova, "High-speed label-free multimode-fiber-based compressive imaging beyond the diffraction limit," *Opt. Express* **30**, 10456–10469 (2022).
- ¹²D. Stellinga, D. B. Phillips, S. P. Mekhail, A. Selyem, S. Turtaev, T. Čížmár, and M. J. Padgett, "Time-of-flight 3D imaging through multimode optical fibers," *Science* **374**, 1395–1399 (2021).
- ¹³Z. Lyu, S.-T. Hung, C. S. Smith, and L. V. Amitonova, "Speckle-based 3D sub-diffraction imaging of sparse samples through a multimode fiber," *APL Photonics* **9**, 126104 (2024).
- ¹⁴T. L. Nguyen, S. Pradeep, R. L. Judson-Torres, J. Reed, M. A. Teitell, and T. A. Zangle, "Quantitative phase imaging: Recent advances and expanding potential in biomedicine," *ACS Nano* **16**, 11516–11544 (2022).
- ¹⁵Y. Park, C. Depeursinge, and G. Popescu, "Quantitative phase imaging in biomedicine," *Nat. Photonics* **12**, 578–589 (2018).
- ¹⁶D. Hillmann, H. Spahr, C. Pfäffle, H. Sudkamp, G. Franke, and G. Hüttmann, "In vivo optical imaging of physiological responses to photostimulation in human photoreceptors," *Proc. Natl. Acad. Sci. U. S. A.* **113**, 13138–13143 (2016).
- ¹⁷Y. Park, W. Choi, Z. Yaqoob, R. Dasari, K. Badizadegan, and M. S. Feld, "Speckle-field digital holographic microscopy," *Opt. Express* **17**, 12285 (2009).
- ¹⁸J. Zhang, S. Dai, C. Ma, T. Xi, J. Di, and J. Zhao, "A review of common-path off-axis digital holography: Towards high stable optical instrument manufacturing," *Light: Adv. Manuf.* **2**, 333–349 (2021).
- ¹⁹G. Zheng, C. Shen, S. Jiang, P. Song, and C. Yang, "Concept, implementations and applications of Fourier ptychography," *Nat. Rev. Phys.* **3**, 207–223 (2021).
- ²⁰L. Tian, J. Wang, and L. Waller, "3D differential phase-contrast microscopy with computational illumination using an LED array," *Opt. Lett.* **39**, 1326–1329 (2014).
- ²¹B. C. Platt and R. Shack, "History and principles of Shack–Hartmann wavefront sensing," *J. Refractive Surg.* **17**, S573 (2001).
- ²²G. Wu, B. Masia, A. Jarabo, Y. Zhang, L. Wang, Q. Dai, T. Chai, and Y. Liu, "Light field image processing: An overview," *IEEE J. Sel. Top. Signal Process.* **11**, 926–954 (2017).
- ²³F. Zhang, G. Pedrini, and W. Osten, "Phase retrieval of arbitrary complex-valued fields through aperture-plane modulation," *Phys. Rev. A* **75**, 043805 (2007).
- ²⁴P. Gao, G. Pedrini, and W. Osten, "Phase retrieval with resolution enhancement by using structured illumination," *Opt. Lett.* **38**, 5204 (2013).
- ²⁵S. Chowdhury and J. Izatt, "Structured illumination diffraction phase microscopy for broadband, subdiffraction resolution, quantitative phase imaging," *Opt. Lett.* **39**, 1015 (2014).
- ²⁶F. Soldevila, V. Durán, P. Clemente, J. Lancis, and E. Tajahuerce, "Phase imaging by spatial wavefront sampling," *Optica* **5**, 164 (2018).
- ²⁷K. Lee and Y. Park, "Exploiting the speckle-correlation scattering matrix for a compact reference-free holographic image sensor," *Nat. Commun.* **7**, 13359 (2016).
- ²⁸Z. Guang, P. Ledwig, P. C. Costa, C. Filan, and F. E. Robles, "Optimization of a flexible fiber-optic probe for epi-mode quantitative phase imaging," *Opt. Express* **30**, 17713 (2022).
- ²⁹J. Sun, J. Wu, S. Wu, R. Goswami, S. Girardo, L. Cao, J. Guck, N. Koukourakis, and J. W. Czarke, "Quantitative phase imaging through an ultra-thin lensless fiber endoscope," *Light: Sci. Appl.* **11**, 204 (2022).
- ³⁰J. Sun, B. Zhao, D. Wang, Z. Wang, J. Zhang, N. Koukourakis, J. W. Czarke, and X. Li, "Calibration-free quantitative phase imaging in multi-core fiber endoscopes using end-to-end deep learning," *Opt. Lett.* **49**, 342–345 (2024).
- ³¹Y. Cotte, F. Toy, P. Jourdain, N. Pavillon, D. Boss, P. Magistretti, P. Marquet, and C. Depeursinge, "Marker-free phase nanoscopy," *Nat. Photonics* **7**, 113–117 (2013).
- ³²V. Micó, J. Zheng, J. Garcia, Z. Zalevsky, and P. Gao, "Resolution enhancement in quantitative phase microscopy," *Adv. Opt. Photonics* **11**, 135–214 (2019).
- ³³M. Born and E. Wolf, *Principles of Optics: Electromagnetic Theory of Propagation, Interference and Diffraction of Light* (Cambridge University Press, Cambridge, 2003).
- ³⁴J. W. Goodman, *Introduction to Fourier Optics* (Roberts and Company Publishers, 2005).
- ³⁵D. C. Ghiglia, "Binary multiplexing and the phase-retrieval problem," *Opt. Lett.* **7**, 602–604 (1982).
- ³⁶S. M. Popoff, G. Leroose, R. Carminati, M. Fink, A. C. Boccara, and S. Gigan, "Measuring the transmission matrix in Optics: An approach to the study and control of light propagation in disordered media," *Phys. Rev. Lett.* **104**, 100601 (2010).
- ³⁷W. Gong, "High-resolution pseudo-inverse ghost imaging," *Photonics Res.* **3**, 234–237 (2015).
- ³⁸L. Song, Z. Zhou, X. Wang, X. Zhao, and D. S. Elson, "Simulation of speckle patterns with pre-defined correlation distributions," *Biomed. Opt. Express* **7**, 798 (2016).
- ³⁹C. Wang, X. Dun, Q. Fu, and W. Heidrich, "Ultra-high resolution coded wavefront sensor," *Opt. Express* **25**, 13736–13746 (2017).
- ⁴⁰J. W. Goodman, *Introduction to Fourier Optics* (Roberts and Company Publishers, 2005).
- ⁴¹M. Plöschner, T. Tyc, and T. Čížmár, "Seeing through chaos in multimode fibres," *Nat. Photonics* **9**, 529–535 (2015).
- ⁴²Z. Lyu, K. Abrashitova, J. F. De Boer, E. R. Andresen, H. Rigneault, and L. V. Amitonova, "Sub-diffraction computational imaging via a flexible multicore-multimode fiber," *Opt. Express* **31**, 11249–11260 (2023).
- ⁴³B. Lochocki, A. Ivanina, A. Bandhoe, J. F. de Boer, and L. V. Amitonova, "Swept-source multimode fiber imaging," *Sci. Rep.* **13**, 8071 (2023).